Applied Thermal Engineering 236 (2024) 121399

Contents lists available at ScienceDirect

Applied Thermal Engineering

journal homepage: www.elsevier.com/locate/ate

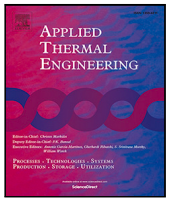

Research Paper

Extended Coherent Flame Model applied to an optical single-cylinder engine fueled with ethanol

Guenther C. Krieger Filho [a,*], Filipi M. Fernandes Silva [a], Antônio L. Pacífico [a], Fernando L. Sacomano Filho [a], Clayton B. Zabeu [b], Francisco B. Nigro [b], Oswaldo M. França Jr. [b], Alexander Penaranda [c], Pedro T. Lacava [c]

[a] Polytechnic School of the University of São Paulo, Av. Prof. Mello Moraes, 2231, São Paulo, 05508-030, SP, Brazil
[b] Instituto Mauá de Tecnologia, São Caetano do Sul, SP, Brazil
[c] Instituto Tecnológico da Aeronáutica, São José dos Campos, SP, Brazil

ARTICLE INFO

Keywords:
ECFM combustion model
Ethanol DISI engine
Optical single-cylinder engine
Ethanol spray

ABSTRACT

One way to achieve a fast track for the decarbonization of the transportation sector is through the usage of biofuels. Among the many biofuels available for transportation, ethanol is one of the most promising, especially when combined with direct-injection spark-ignited engine technologies. The present work aims to validate 3D Computation Fluid Dynamics (CFD) ethanol spray and combustion models with the calibration of specific model parameters using experimental data obtained with optical measurements. Focus is given on the investigation and determination of the Extended Coherent Flame Model parameters for hydrous ethanol turbulent spray combustion. To characterize the spray produced by the injector, measurements obtained with a Phase Doppler Interferometer system are used. Natural luminosity and in-cylinder pressure are acquired on a single-cylinder research engine with optical access. The work also considers results obtained from 1D and 3D CFD models to supplement the acquired experimental setup. From the comparison between experimental and numerical results, it comes out that a correction of the Extended Coherent Flame Model turbulence stretch parameter can be done according to a ratio of flow and combustion length scales obtained at the spark time. In this sense, an expression is proposed to allow the correction of such a parameter in different engine operating conditions. Accordingly, in-cylinder mean effective pressure calculated with 3D CFD simulations show a good agreement with the experimental data for all studied cases.

1. Introduction

The transport sector is one of the main sources of greenhouse gases (GHG) and it requests, therefore, the development of new engine technologies able to minimize CO_2 emissions. One way to achieve a fast track in the decarbonization of transportation sector is by the utilization of biofuels [1], in which ethanol stands out. Ethanol receives a special attention when combined direct injection (DI) engines technologies, because of the resulting positive aspects which are not limited to GHG mitigation but also include improvements of engine efficiency. However, the usage of ethanol has some characteristics which clearly demand specific investigations, for instance: (1) when compared to gasoline, ethanol presents higher knock resistance and higher values of laminar flame speed and heat of vaporization [2]; (2) its low heating value (LHV) per mass unit is lower than gasoline, which leads to a higher volumetric fuel consumption; (3) in regard of the vaporization process, its latent heat of vaporization is almost three times higher than pure gasoline and it does not present a vaporization curve like gasoline with lighter compounds vaporizing at low temperatures [3]; (4) ethanol has a hygroscopic behavior, which allows condensation of water vapor onto the droplet surface [4]. These aspects have a strong impact on spray formation and droplet evaporation which also may contribute to formation of liquid film on chamber walls [5] and may pose difficulties to cold engine start [6]. Hence, for the development of more advanced ethanol DI engines, there is still a need for more technological and phenomenological studies.

Although ethanol has become a popular fuel for ICEs, the literature related to the topic is not extensive. The usage of pure and hydrous ethanol is predominantly found in experimental studies [3,7–10] that in some cases include numerical simulations [6,11–13] as well. More applications are found when fuel blends including ethanol are considered [6,12–18]. Altogether, applications cover a broad range of operating strategies, e.g. port-fuel injection [11,19], compression

* Corresponding author.
E-mail address: guenther@usp.br (G. C. Krieger Filho).

https://doi.org/10.1016/j.applthermaleng.2023.121399
Received 7 January 2023; Received in revised form 8 August 2023; Accepted 17 August 2023
Available online 25 August 2023

Abbreviations

AMR	Adaptative Mesh Refinement
ASOS	After Start of Sparking
BDC	Bottom Dead Center
CFD	Computational Fluid Dynamics
CMOS	Complementary Metal-Oxide Semiconductor
COV-IMEP	Covariance of Indicated Mean Effective Pressure
DDM	Discrete Droplet Model
DI	Direct Injection
DISI	Direct-Injection Spark-Ignition
DOI	Duration of Injection
ECFM	Extended Coherent Flame Model
EDI	Ethanol Direct Injection
EER	Ethanol Energy Ratio
EVO	Exhaust Valve Opening
FGM	Flamelet Generated Manifold
GCI	Grid Convergence Index
GHG	Greenhouse Gases
GPI	Gasoline Port Injection
ICE	Internal Combustion Engine
IMEP	Indicated Mean Effective Pressure
ITNFS	Intermittent Turbulence Net Flame Stretch
IVC	Intake Valve Closure
KH	Kelvin–Helmholtz
LHV	Low Heating Value
MFB	Mass Fraction Burned
PDF	Probability Density Function
PIV	Particle Imaging Velocimetry
RANS	Reynolds Averaged Navier–Stokes
RHR	Rate of Heat Release
RNG	Re-Normalization Group
RT	Rayleigh–Taylor
SCRE	Single Cylinder Research Engine
SI	Spark-Ignition
SMD	Sauter Mean Diameter
TDC	Top Dead Center
TPA	Three Pressure Analysis

Symbols

a_P	model parameter
a_T	model parameter
B_m	model parameter
B_ϕ	model parameter
C_{surf}	model parameter
D	flame surface destruction due to fresh gas consumption, 1/(ms)
K_t	ITNFS term, Eq. (2)
m_P	model parameter
m_T	model parameter
P_1	flame surface production by turbulent stretch, 1/s
P_2	flame surface production by mean flow dilatation, 1/s
P_3	flame surface production by flame thermal expansion and curvature, 1/s
P_k	source term applied during the ignition period by spark plug
p	pressure, Pa
S	surface area, m^2
$S_{bg,ign}$	representative surface area of the burned gas ignited, m^2
s_l	laminar flame speed, m/s
T_u	unburnt gas temperature, K
t	time, s
$\tilde{u}$	favre averaged velocity, m/s

Greek Symbols

α_t	model parameter
β	model parameter
γ	model parameter
μ	mean dynamic viscosity, kg/(ms)
μ_t	turbulent dynamic viscosity, kg/(ms)
ρ	density, kg/m^3
Σ	flame surface density, 1/m
ϕ	fuel/air equivalence ratio
$\overline{\phi}$	average value of the fuel/air equivalence ratio
ϕ_m	model constant

Non-dimensional terms

Sc	Schmidt number
Sc_t	turbulent Schmidt number

Subscript

ref	reference value
exp	experimental
CFD	Computational Fluid Dynamics

ignition engines [12,13,20], and direct injection [3,5,6,8,9,14]. As this work concentrates on DI engines, special attention is given to this technology hereafter.

When considering experimental investigations, the work of Aleiferis et al. [8] stands out. In that work, a comprehensive study was conducted about the combustion process in an optical access DI, SI engine fueled with gasoline, iso-octane, ethanol, and butanol (methane was used as benchmark for the other fuels). With respect to the ethanol, this fuel exhibited higher peak pressure and fastest mass fraction burned (MFB). Similar observation is also noticed in [3]. Concerning the flame growth at the ignition timing, ethanol was demonstrated to be the fastest. Koupaie et al. [9] investigated ethanol in a central direct injection spark ignition engine aiming to improve understanding and specifically quantify the direct influence of water content on the hydrous ethanol fuel on the flame propagation event in terms of apparent bulk flame distortion and centroid migration inside the combustion chamber. Several flame related parameters, such as shape factor and apparent flame speed, are discussed and compared with the flow and heat release analysis. At the end, it was concluded pure ethanol and hydrous-ethanol (20% water content) were the fastest and the slowest burning fuel respectively. Focusing more on the spray formation, Bao et al. [2] studied the spray development of ethanol, gasoline and iso-octane in an optically accessible, DISI engine. Additional investigation was conducted in a constant-flow spray chamber. In both devices, high-speed Mie-scattering imaging is performed to measure penetrations of spray plumes at various injection pressures ranging between 4 and 15 MPa. The results show that the effect of fuel type on the tip penetration length of the sprays depends on the injection conditions and the level of fuel jet atomization and droplet breakup. Such aspects were also noticed in [5] in terms of non reacting flow simulations of different DI hydrous ethanol strategies in DISI engines. The results obtained in [5] showed that injection pressures as well as start of injection

are parameters, which influence directly the fuel vaporization, and the amount of wall-wet fuel film formed mainly on piston. This emphasizes the importance of the detailed description of spray injection for a careful CFD simulation as presented here. In this sens, it is important to mention that, although comprehensive experimental evaluation of both penetration length and penetration rate are conducted in [2], no measurement is done on droplets SMD and velocities, which are necessary inputs for spray simulations.

Huang et al. [6] and Zhuang et al. [14] combines experimental and numerical investigations for a single cylinder naturally aspirated motor-cycle engine fired with gasoline and ethanol. In both works, numerical simulations have been conducted within the RANS (Reynolds Averaged Navier–Stokes) approach for the turbulent flow description coupled with the Extended Coherent Flame Model (ECFM) combustion model. [6] investigate the effect of ethanol direct injection plus gasoline port injection (EDI+GPI) on charge cooling effect and combustion characteristics. Simulation results of E100 operating in DI presented low adherence with the achieved experimental data. Concerning the ethanol spray modeling, the validation was limited to the evaluation of penetration length and spray envelope angle. Zhuang et al. [14] focused on the engine performance, considering a similar setup from that used in [6]. It was shown that, combustion process was improved by EDI when ethanol energy ratio (EER) was less than 42%, however further increase of EER led to the deterioration of combustion process, mainly due to over-cooling and poor mixing of the ethanol. The numerical setup was the same as [6] and, in both works, any specific analysis of the ECFM model parameters has been presented.

Still within the context of DI engine simulations fueled with ethanol, other strategies have been chosen to address the turbulence flame interaction. Giramondi et al. [13] adopted the β-PDF approach coupled with the flamelet generated manifold (FGM) chemistry reduction technique to investigate the ignition dynamics of an ethanol-diesel direct injection compression ignition engine. Experimental results of a previous test campaign on a single-cylinder research engine equipped with two direct injectors are used to validate the CFD model. The in-cylinder pressure and apparent rate of heat release traces computed in the simulations are found to be consistent with the corresponding experimental results. In contrast, Battistoni et al. [11] considered a detailed chemistry approach without any turbulence-chemistry interaction model to investigate an spark-ignited (SI) optical access engine using gasoline and ethanol as fuels. The authors justify this approach by the fine mesh resolution on the reaction zone. However, the authors show that grid independence may be not have been achieved for the chemical source term. In-cylinder pressure, heat release, and flame morphology have been compared with experimental data. Although there is no validation for more than one IMEP, results indicate that simulations are able to predict experimental data with good agreement. Variations due to changing fuel type and air-fuel ratio are well captured, with some limitation for the prediction of the indicated pressure, where low adherence has been noted with the experimental data. A perfect premixed air-fuel mixture is admitted at the inlet boundary. The engine is operated at part load, and the throttle is included in the 3D domain. Boundary conditions, consisting basically of static pressure and temperature for the inflow, and static pressure for the outflow, have been derived from experiments.

Within the context of DI engines fueled with ethanol, this work presents the validation of 3D CFD spray and IC-engine modeling strategies and proposes a methodology to calibrate specific combustion model parameters. Experimental data acquired from spray injections into quiescent atmospheres and an optical single cylinder engine have been used to accomplish this task. Special efforts have been made to well represent the required boundary conditions for the CFD simulations. The Extended Coherent Flame Model (ECFM) [21,22] is adopted to simulate the combustion process of ethanol DISI engine in the present work. Focus is given on the investigation and determination of the ECFM parameters which could be applied to a 3D CFD model of an ethanol direct-injection, spray-guided, spark-ignited engine. As shown in the results section standard parameter values are not able to describe a full range of engine operation. The main goal is to have the combustion model calibrated to both full and part load operation, as well as at high and low speeds.

Table 1
Engine specifications.

Engine type	single cylinder, water cooled, 4-stroke, DI
Displacement	475 cm^3
Bore x stroke	90 mm x 82 mm
Piston cold diameter	80.5 mm
Nominal compression ratio	9.27:1
Intake valve timing	open 348°; close 573° (After fired TDC)
Exhaust valve timing	open 129°; close 377° (After fired TDC)

2. Materials and methods

The methodology applied in this work evolves in four stages. First, experimental measurements are done in an optical access single cylinder engine to deliver the reference data for simulations. Second, experimental measurements of the employed injector are performed to assist the simulations in regard of the specification of spray injection conditions. Third, 1D simulations follow the process to define inaccessible information of the experimental data. Finally, analyses of 3D CFD model parameters are conducted in order to improve the prediction ability of the chosen modeling technique. As further specified, iterations between 3D CFD and 1D simulations exists, which is indispensable for the entire modeling refinement.

2.1. Single-cylinder research engine

Experiments were performed on an optically accessible single-cylinder direct injection SI engine, coupled to an active AC dynamometer available at Technological Institute of Aeronautics (ITA) in São Paulo, Brazil. The cylinder head has four valves and a spark plug which is located 5 mm from the center of the combustion chamber in the direction of the exhaust side. For these experiments, the cylinder liner was replaced by a quartz window to offer a lateral view of the combustion chamber. Additionally, the piston provided a sapphire window which replaced the piston bowl with flat bottom. Both setups enabled the passage of optical signals coming from the combustion chamber, making it possible to study the combustion process [23,24] with optical techniques. The Fig. 1 shows an overview of the test bed configuration and the engine specifications are shown on Table 1.

Tests were carried out for the operational conditions shown on Table 2. The chosen operational points represent the engine at full and partial loads as well as at high, middle, and low rotational speeds.

For each experiment the following procedure was executed: initially the engine was operated in motored condition to setup the engine speed and intake air flow. Before the engine is fired it was checked that the exhaust temperature was below < 343 K. The engine was operated in fired condition up to the defined relative air fuel ratio is reached and stabilized, and consequently 150 cycles were recorded. Because the exhaust temperature is still rising before turning off the fuel injection, it is used the optical data of the last recorded cycle. After the experimental recording, the fuel injection is turned off and the engine was stopped for cleaning the optical piston, and cylinder liner. The number of cycles ran and the recorded cycle, used as reference cycle in both 1D and 3D CFD simulations, are shown on Table 3.

Spark advance timing was setup to provide the maximum Indicated Mean Effective Pressure and a stable operation for all operating conditions (COVIMEP < 1.5%). The duration of injection (DOI) was set to achieve the relative air-fuel ratio (λ) value imposed for each test; the latter parameter was measured using a wide-band exhaust gas oxygen sensor installed at the exhaust manifold, with an integrated ETAS ES630 lambda module (uncertainty of ±1%). The start of injection was

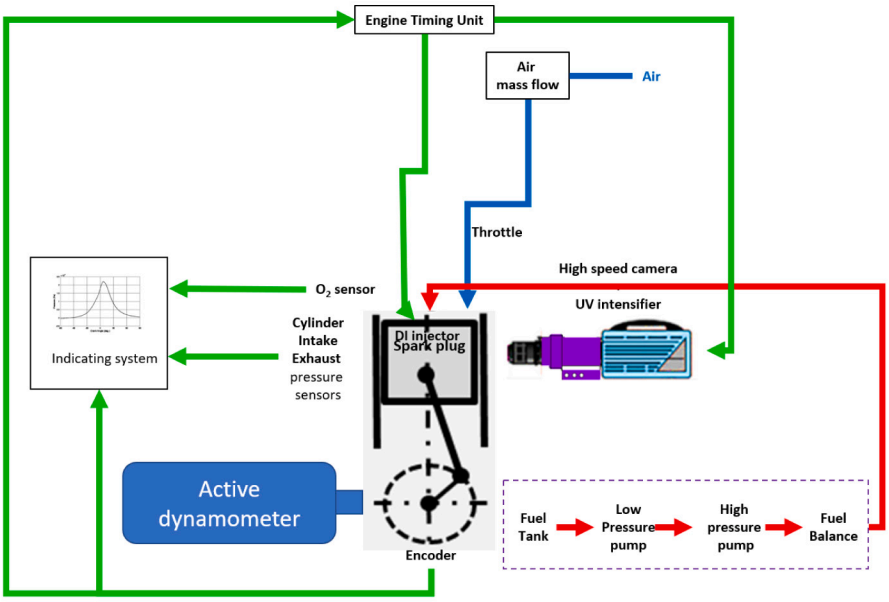

Fig. 1. Experimental arrangement for the optically-accessible single-cylinder engine.

Table 2
Experimental engine operational conditions.

	Case 1	Case 2	Case 3	Case 4	Case 5	Case 6
Engine speed [rpm]	2000	900	2500	2500	2000	900
IMEP [bar]	4.99	5.02	5.06	3.07	3.02	3.03
IMEP dev. [bar]	±0.16	±0.28	±0.10	±0.08	±0.08	±0.09
SOI [CAD bTDC]	290	290	290	290	290	290
DOI [CAD]	53.64	27.65	66.75	45.00	37.20	20.06
Inj. Pressure [bar]	100	100	100	100	100	100
Spark timing [CAD bTDC]	14	6	16	16	14	12

Table 3
Identification of ran and reference cycles.

	Case 1	Case 2	Case 3	Case 4	Case 5	Case 6
Cycles ran	275	299	239	213	209	112
Reference cycle	275	299	239	209	208	110

Table 4
Test fuel properties - hydrated ethanol.

Chemical formula	C_2H_5OH
Density@20 °C [kg/m3]	0.81150
RON	110
Stoichiometric air/fuel ratio	8.5322
LHV [MJ/kg]	24.76
Enthalpy of vaporization [kJ/kg]	902
Boiling temperature [K]	350

fixed during the intake stroke at 290 crank angle degrees before top dead center firing. Engine lubricant oil and coolant temperatures were fixed at 333 K by means of an external temperature conditioning unit; ambient pressure was 0.95 bar and intake air temperature was around 308 K.

The crankshaft rotational speed was controlled by an active dynamometer that stabilizes the speed with an uncertainty of ±1%. The load was controlled by adjusting the intake throttle so as to maintain a constant value of the indicated mean effective pressure (IMEP), calculated from in-cylinder pressure measurements.

The engine was fueled with a blend of 95% of anhydrous ethanol and 5% of water on a volume basis. The blend percentages were validated using a Rudolph Research Analytical density meter DDM 2911. The engine was operated in stoichiometric conditions, and Table 4 shows the main properties of the fuel used in this study.

Measurements of in-cylinder pressure was done by means of a piezoelectric pressure transducer flush-installed in the region between the intake and exhaust valves, with an estimated uncertainty of ±1%. Intake and exhaust pressure transducers were installed in intake and exhaust manifolds. These pressures were measured according to the crankshaft position using an angle encoder with a crank angle resolution of 0.1 CAD. The intake air mass flow was measured by an ultrasonic transit-time difference method using an ultrasonic transducer located 6.0 meters from the intake port with a sampling rate of 10 Hz. For the experiments, a fuel system was utilized, containing a 10 l tank, a 4 bar fuel pressure pump, a fuel balance AVL model 733S integrated with a fuel temperature conditioner and a high-pressure fuel pump controlled by an AVL REPMS control unit. This system supplied fuel at a constant injection pressure of 100 bar, temperature of 303 K, to a direct injector of the Bosch model 0261 500 103, which was positioned in the center of the combustion chamber.

The time resolved visualization of the combustion process was done from the lateral view of the cylinder head using a high-speed PCO.dimax S1 (CMOS) camera with a UV-Nikon 105 mm f/4.5 lens. In order to improve the spray visualization two led lamps were strategically positioned outside the quartz cylinder liner.

2.2. Injector and spray characterization

In order to setup the injector and spray model, PDI technique is applied to characterize the fuel spray. The injector model is validated upon an spray in open and quiescent environment, as shown in Appendix A. Following this strategy, injector model parameter SMD =

30 μm, q = 6, and cone angle = 20° are determined for the 3D CFD simulation. The injection pressure, 100 bar, was the same for both open spray on quiescent atmosphere and single cylinder research engine.

2.3. 1D model

An 1D model is applied in order to provide unavailable and inaccessible experimental data to the 3D CFD model. For instance, the experimental setup does not provide direct measurement of the mass flow neither at the same location (close to both inlet and outlet ports) where pressure transducers are positioned nor with high enough CAD resolution. Therefore, an 1D Models is built and applied to describe the engine operation and to provide the remaining data required for the 3D CFD model, i.e.: mass flow, inlet and outlet temperatures, and outlet pressure. More details are available in Appendix B.1.

During the model calibration, there was an iterative procedure between 3D CFD and 1D models. The 3D CFD model provides information about the spray evaporation rates and the evaporation mechanism: free spray or liquid film evaporation. The valve discharge coefficient, used in the 1D model, was evaluated by means of a 3D CFD simulation of a flow bench with the same cylinder head and valves geometries. Further details of this procedure and data are on Appendix B.2.

2.4. 3D CFD simulations

To perform the CFD simulations, the CONVERGE CFD software package [25] version 3.1.6 was used. The so-called Extended Coherent Flame Model (ECFM) [22] is chosen to describe the reacting flow. It is important to mention that no modifications on the original implementations of the model have been conducted in the present study.

The computational domain and mesh are shown in Fig. 2. The domain is composed by an intake region (intake ports and valves), a cylinder region (piston with crevice, liner, head and spark plug) and an exhaust region (exhaust valves and ports).

An orthogonal base grid of 4 mm is employed. Converge CFD uses a cut-cell methodology to generate the mesh on the fly applying refinement rules defined by user. The grid size is reduced to 1 mm throughout the entire combustion chamber and exhaust ports. The mesh has a size of 0.5 mm around the intake and exhaust valves all the time, except during gas exchange, when mesh size reaches 0.25 mm. Mesh drops to 0.5 mm during injection and spark, as well. Also, adaptive mesh refinement (AMR) is used in the model to refine the mesh based on the gradients of temperature and velocity. Grid independence study is shown on Appendix C.

The turbulent flow was modeled within the RANS approach considering the RNG-k-ϵ model. DI spray was simulated via Discrete Droplet Model (DDM) according to Eulerian–Lagrangian droplet parcels approach and the Rosin-Rammler distribution method was used to setup the droplet initial diameter in agreement with the acquired experimental data (details in Appendix A). The liquid atomization and drop breakup were based on the Kelvin–Helmholtz (KH) and Rayleigh–Taylor (RT) instability mechanisms. In the used KH-RT model, aerodynamic instabilities (i.e., KH waves) are responsible for the primary breakup of the injected liquid blobs (also known as parents). Child drops are created during this process, and the secondary breakup of these drops is modeled by examining the competing effects of the KH and RT mechanisms. The turbulence interaction between droplets and gaseous flow is based on the O'Rourke distribution model. All of these models are adequately described and well-used in the literature. Table 5 brings a summary of model setup.

The combustion process is described by the evolution of the Flame Surface Density, Σ, according to its transport equations, Eq. (1):

$$\frac{\partial \Sigma}{\partial t}+\frac{\partial \tilde{u}_i \Sigma}{\partial x_i}=\frac{\partial}{\partial x_i}\left(\left(\frac{\mu_t}{Sc_t}+\frac{\mu}{Sc}\right)\frac{\partial \Sigma/\rho}{\partial x_i}\right)+\left(P_1+P_2+P_3\right)\Sigma-D+P_k \quad (1)$$

Table 5
Computational models.

Turbulence	RNG-k-ϵ [31]
Heat transfer	wall treatment [29]
Fuel spray	Discrete Droplet Model [25]
Initial droplet distribution	Rosin-Rammler distribution method, and PDI measurements: SMD = 30 μm, q = 6, and cone angle 20°
Primary and Secondary breakup	KH-RT [32]
Droplet turbulent dispersion	O'Rourke model [33]
evaporation	Frossling model [33]
spark model	ISSIM [28]
combustion	ECFM-SB [22]

In Eq. (1), the term P_1 takes into account the flame surface density production caused by the turbulent stretch, whereas the term P_k is the source term applied during the ignition period by the spark plug. The physical meaning and modeling of the terms P_2, P_3, and D can be seen on [26]. The flame surface production by turbulent stretch term is modeled [22] as

$$P_1=\alpha_t K_t \Sigma, \quad (2)$$

where K_t is the ITNFS stretch term [27] and α_t its modeling parameter.

The initial flame surface density production caused by the spark plug is modeled [25,28] as

$$P_k=max((C_{surf}S_{bg,ign}-\Sigma)dt^{-1},0), \quad (3)$$

where C_{surf} is a model parameter and $S_{bg,ign}$ is a representative surface area of the burned gas ignited by the spark plug.

The energy conservation equation used in CONVERGE is presented in the form of absolute specific internal energy of the gaseous mixture. Therefore, the net heat release associated to the combustion reactions is not included. Such a term would appear if the sensible internal energy were used. The boundary conditions for the specific internal energy conservation equation are presented in Table 6. For each wall, a temperature value is prescribed. For inlet and outlet ports, temperature values, for each CAD, are prescribed based on the 1D model results. In order to model the turbulent thermal boundary layer, a wall heat transfer model [29] is applied.

According to the ECFM, effects of chemical reactions are taken into account by means of the laminar flame speed, namely through the terms P_1, P_3 and D. The ethanol laminar speed proposed by [30] is adopted to account for variations of the laminar flame speed according to the mixture composition, pressure and unburnt gas temperature as given in Eq. (4).

$$s_l=s_{l,ref}\left(\frac{T_u}{T_{u,ref}}\right)^{\gamma}\left(\frac{p}{p_{ref}}\right)^{\beta} \quad \text{with} \quad s_{l,ref}=B_m+B_\phi\left(\tilde{\phi}-\phi_m\right) \quad (4)$$

where parameters B_m, B_ϕ, and ϕ_m are respectively set to 45.7 cm/s, −1.3cm/s, and 1.11 to account for ethanol combustion. In Eq. (4), ϕ is the equivalence ratio, p the pressure, T the temperature, the subscript ref indicates reference values, $\gamma=a_T+m_T(\phi-1)$ and $\beta=a_P+m_p(\phi-1)$, where $a_T=1.75$, $m_T=-0.271$, $a_P=-0.17$, $m_P=0.14$.

Apart from the influence of the ethanol laminar speed, this work investigates the terms P_1 and P_k for ethanol DISI engines. According to [26], the term P_1 has a major impact on the flame surface production in any internal combustion engines.

The boundary conditions used at the 3D simulation were gathered from: (a) experimental measurements on the SCRE test bed, (b) calculated values using 1D model and (c) assumed values. The crank angle resolved values of the intake mass flow rates, intake temperature, and exhaust pressures calculated with the 1D model (see Appendix B.1) are imposed as boundary conditions to 3D CFD model. Temperatures of the combustion chamber, valves, ducts and crevice boundaries are set according to some literature references for SCRE. These details are provided in Table 6. Eq. (1) is solved only for the CAD interval when

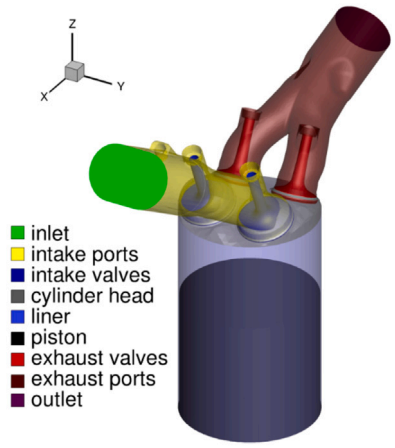

(a) SCRE computational domain. For details on Intake and Exhaust boundary conditions, see Appendix B

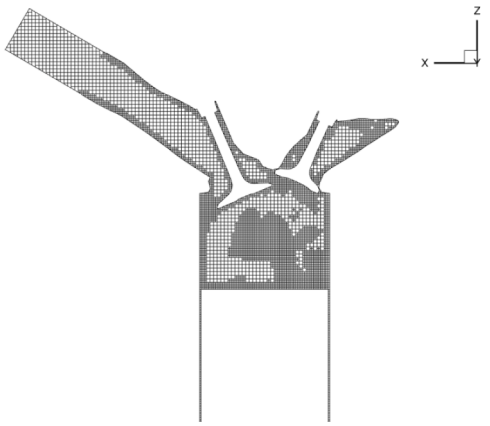

(b) Mesh at valve plane

Fig. 2. Computational domain and grid.

Table 6
Boundary conditions.

Boundary	Temperature [K]	Mass flow [kg/s]	Pressure [MPa]	Mass fraction N2/O2/	I_t [–]	Length scale [m]
Piston top	450	–	zero gradient	zero gradient	zero gradient	zero gradient
Head	500	–	zero gradient	zero gradient	zero gradient	zero gradient
Cylinder liner	450	–	zero gradient	zero gradient	zero gradient	zero gradient
Exhaust valve bottom	610	–	zero gradient	zero gradient	zero gradient	zero gradient
Exhaust port angle	525	–	zero gradient	zero gradient	zero gradient	zero gradient
Intake valve bottom	550	–	zero gradient	zero gradient	zero gradient	zero gradient
Intake port angle	425	–	zero gradient	zero gradient	zero gradient	zero gradient
Inflow	from experiment/ 1D Model	from experiment/ 1D Model	zero gradient	0.79/0.21	0.02	0.003
Outflow	zero gradient	zero gradient	from experiment/ 1D Model	zero gradient	0.02 (backflow)	0.003 (backflow)

Table 7
Fuel injection.

	Case 1	Case 2	Case 3	Case 4	Case 5	Case 6
DOI (CAD)	53.64	27.65	66.75	45.00	37.20	29.06
Injected mass (mg)	39.72	51.20	44.50	25.07	26.67	21.00

all valves are closed, in other words, the flame surface density equation is only solved for the trapped mass. Therefore, its boundary condition is zero gradient in all walls of the computational domain.

The fuel injection time and fuel mass were obtained from the test bed and are shown in Table 7. Further details on the fuel injection setup can be seen on Appendix A.2.

3. Results and discussion

In this section, results obtained from both experimental measurements and numerical simulations are presented and discussed in three parts. The first is dedicated to in-cylinder pressure curves achieved experimentally and with the 1D model. Next, results achieved with 3D numerical simulations and standard methods are showed and defined as references for further analysis. Experimental results are also included in this second part to supplement the conducted discussions. Finally, the third section is dedicated to the procedure used to calibrate the ECFM parameters.

3.1. In-cylinder pressure curves for full and partial loads

The full load in-cylinder pressure against displaced volume are shown in Figs. 3(a), 3(c), and 3(e), whereas the partial load data are shown in Figs. 3(b), 3(d), and 3(f). This type of cycle representation allows one to easily identify the four engine strokes: the two lines at the bottom are admission (pressures below the atmospheric pressure) and exhaust strokes. The compression stroke is the almost straight line, where the pressures increases from the atmospheric to the end-compression pressure. The combustion process, close to the TDC, increases the pressures to the cycle peak pressure. The expansion stroke indicates the pressure trace decreasing from the peak pressure until the blowdown pressure, where the exhaust valves open, close to the BDC. Alongside the experimental data, the 1D model results are also included.

The chosen operational points – 6 cases – stress the computational model for spray ethanol turbulent combustion. The high, middle, and low rotational speeds influence the turbulent flow and, as a consequence, the flame wrinkling. On the other hand, the engine loads –

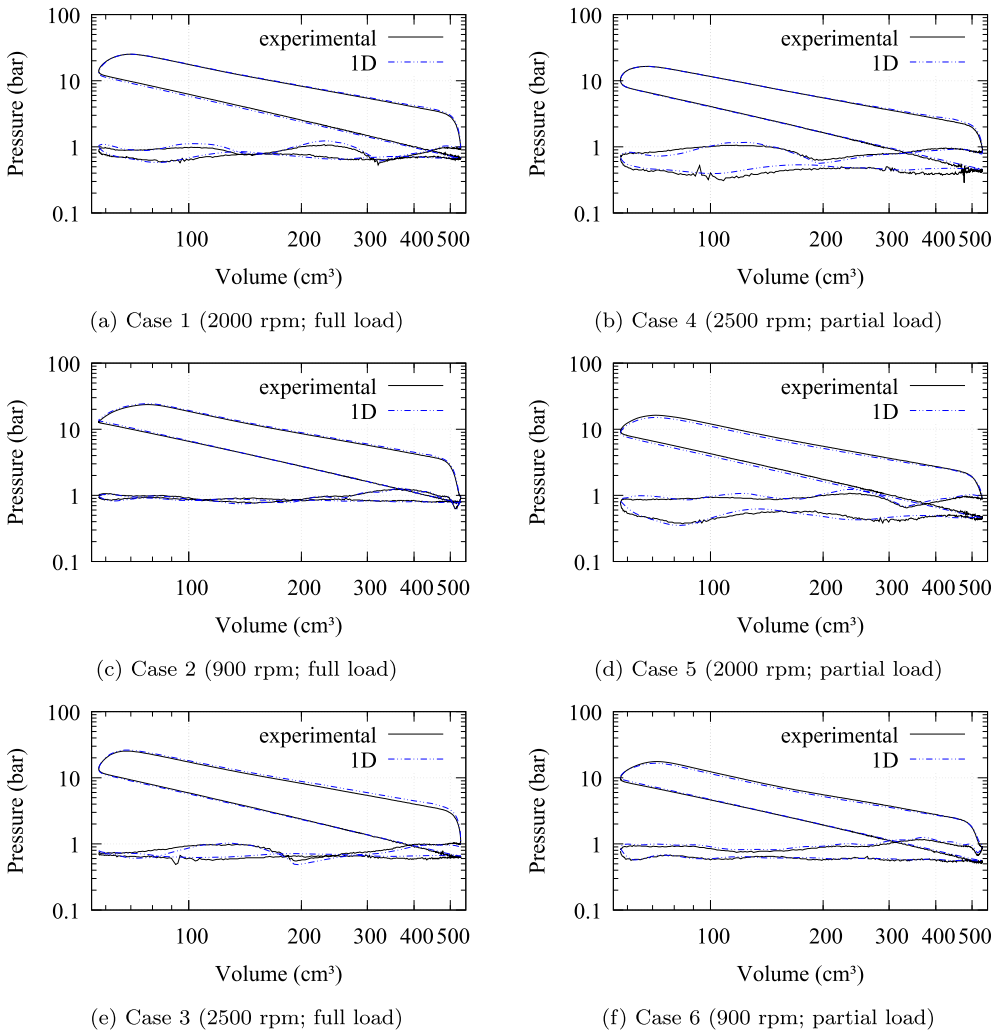

(a) Case 1 (2000 rpm; full load)

(b) Case 4 (2500 rpm; partial load)

(c) Case 2 (900 rpm; full load)

(d) Case 5 (2000 rpm; partial load)

(e) Case 3 (2500 rpm; full load)

(f) Case 6 (900 rpm; partial load)

Fig. 3. In-cylinder pressures versus displaced volume for full load (5 bar IMEP) cases (a), (b) and (c); and for partial load (3 bar IMEP) cases (d), (e) and (f). Experimental data (solid line), 1D Model results (dashed line). The uncertainty of the piezoelectric pressure sensor is +/ − 1%.

full and partial – impart the mixture formation because of both time and amount of injected fuel. One has to keep in mind, however, there are crossed influence of rotational speed and load on the turbulent combustion process.

On Fig. 3 one can see peak pressure values of about 25 bar and 17 bar at full and partial load cases, respectively. For the partial load cases, it is also possible to identify on Figs. 3(b), 3(d), and 3(f), at the lower part of the graphs, because of the throttling, the in-cylinder pressure falls down to about 0.4 bar. As a consequence, the pumping work is higher at partial load than at full load when compared with the compression/expansion work. The combustion process, which occurs at the end of the compression stroke or around the TDC, is discussed with more details at the following sections.

The typical pressure oscillations during the gas exchange process, at both admission and exhaust strokes, are depicted on the lower part of the graphs on Fig. 3. The 1D model reproduce the experimental pressure traces with high accuracy. As already mentioned on Sections 2.3 and 2.4, it was used an iterative procedure to exchange data between 1D and 3D CFD models. During this iterative process, the most sensitive quantities are the mass flow rate, inlet and outlet pressures, fuel droplets evaporation rates and energy source (gaseous mixture or walls) for the evaporation process as well as the combustion heat release profile. Applying such an iterative procedure, the 1D model recovers not only the pressure traces, indicated on Fig. 3, but also produce valid complementary boundary conditions necessary in the 3D CFD simulation. For more details see Section 2.3 and Appendix B.

For all the measured cases shown on Fig. 3, the curve section associated with the expansion stroke, following the combustion end, cannot be represented by a straight line. Namely, the polytropic exponent is not constant. Although further investigations about this last issue is beyond the scope this work, two possible causes can be listed: (a) higher heat transfer rate at the glass cylinder wall in comparison to the heat transfer rate at the metal engine block during the final part of the expansion stroke; (b) post combustion of the mixture returning from the crevice to the main chamber.

3.2. 3D numerical simulation

The studied engine operational points are expected to influence both the mixture formation and turbulent combustion process. Therefore, the studied cases are deemed useful to calibrate the ECFM for ethanol combustion.

As already mentioned in Section 2.4, the most important contribution to the flame surface density development comes through the term P_1 on Eqs. (1) and (2). As an initial attempt to calibrate the model, the constant $\alpha_t = 0.8$ is fitted to the case 1 and applied to all other studied cases.

Results of temperature fields achieved from the 3D CFD numerical simulation are compared with the natural luminosity of the flame achieved from experiments for the case 1 in Fig. 4. A good agreement between simulation and experiment can be noticed for the flame

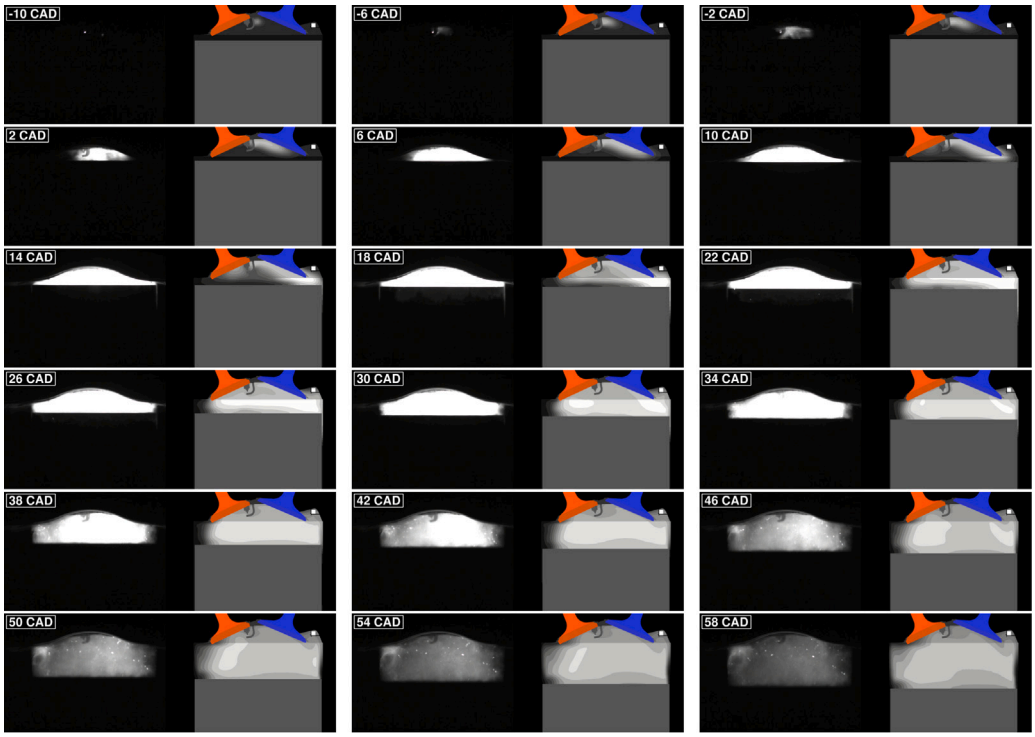

Fig. 4. Flame development on a middle longitudinal plane. Natural luminescence measurements (left) and temperature field from 3D CFD simulation $\alpha_t = 0.8$ (right) for case 1.

growth in a qualitative fashion: the flame propagates initially to the right (2-10 CAD) and combustion takes place even inside the crevice (18-22 CAD). Once natural luminosity does not correspond exactly to the mixture temperature, further quantitative comparison is not possible.

A quantitative evaluation of the quality of the numerical simulation against experiments is done upon the in-cylinder pressure traces for the studied cases. The results for the cases 1, 2 and 6 are shown in Fig. 5. For the three cases, the 3D CFD simulations reproduce the admission, compression and exhaust strokes very well. The combustion process for the case 1 is well reproduced, because the $\alpha_t = 0.8$ parameter was fitted to this case. For the case 2, at full load as case 1, the adherence at the combustion process is good. However, it is easy to see that for the case 6, a partial load case, the simulation does not reproduce the experimental combustion process and, as a consequence, the expansion stroke. In order to investigate such deviations, natural luminescence and rate of heat release rate obtained from experiments for cases 1, 2 and 6 are compared.

The 3D CFD simulated pressure traces indicate a low intensity combustion for the partial load cases. The natural luminescence of the flame related to cases 2 and 6 are shown on Fig. 6. Both cases have same engine speed (900 rpm), but full (5 bar IMEP) and partial load (3 bar IMEP), respectively. The angle on the images are referred to the angle of start of sparking – ASOS means After Start of Sparking – of each case. Based on the images intensities for 54 to 74 ASOS, one observes the combustion process lasts longer on case 2.

The rate of heat release (RHR) for cases 1, 2, and 6 are evaluated based on the experimental data. The results are shown on Fig. 7. The peak of the RHR for cases 1 and 2 are quite similar, about 29 J/CAD, and for case 6, about 20 J/CAD. Furthermore, the positive slope of the RHR until 20 ASOS is higher for cases 1 and 2. This means the combustion development is faster for cases 1 and 2 than for case 6. Therefore, a constant parameter $\alpha_t = 0.8$ cannot reproduce all the studied cases.

3.3. Extended coherent flame model parameter investigation

As concluded in the previous section, a constant value for the flame surface density wrinkling parameter - α_t - cannot reproduce partial and full load cases. This conclusion motivated the investigation of ECFM parameters under the perspective of a sensitivity analysis. Herein, a physically meaningful ordinary linear equation was empirically sought to allow the calibration of the model parameter α_t for the DISI ethanol studied cases. To accomplish this task, theoretical knowledge related to the propagation of turbulent flames was considered to define the independent parameters for the sought equation.

As already mentioned in the literature [13], turbulent transport is likely to play a more relevant role compared to the swirl bulk motion on the propagation of ethanol flames. Therefore, a sensitivity analyses on the stretch parameter is carried out. The outcome of the sensitivity analysis is twofold: a) the model constant C_{surf} related to the initial flame surface density production rate can be kept constant for all simulated cases. b) the stretch parameter, α_t, scales as function of the turbulent integral length scale, L, and laminar flame thickness, δ_l, as $\alpha_t = c_1 \frac{L}{\delta_l} + c_2$. The constants c_1 and c_2 are evaluated based on the α_t values for the cases 1 and 6, because these two cases span the range of $\frac{L}{\delta_l}$. The parameter $\frac{L}{\delta_l}$ for the six studied cases are shown on Table 8.

The results obtained with corrected α_t are shown on Fig. 8. For the partial load cases, the better agreement between experimental and numerical pressure traces is evident.

A quantitative evaluation of the proposed ECFM parameter calibration is done based on the IMEP of all six cases. On Table 9, the influence of the α_t, and consequently P_1, on the calculated IMEP for the six studied cases is shown. Results for both constant and calibrated α_t are presented. The absolute deviations, between simulation and experiment, for each case and α_t are indicated. The average value for the absolute deviation, calculated with the six cases, is 9.83% and 4.41% for constant and corrected α_t respectively. If only the low load cases (3 bar IMEP) are taken into account, the average value for the deviations for constant and corrected α_t are 16.34% and 3.72% respectively.

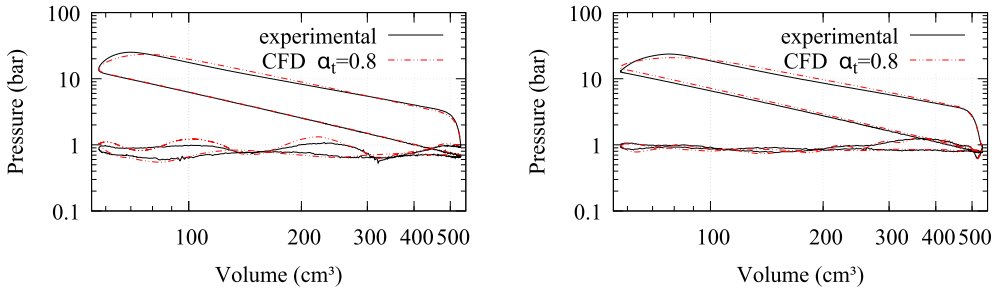

(a) Case 1 (2000 rpm; full load) (b) Case 2 (900 rpm; full load)

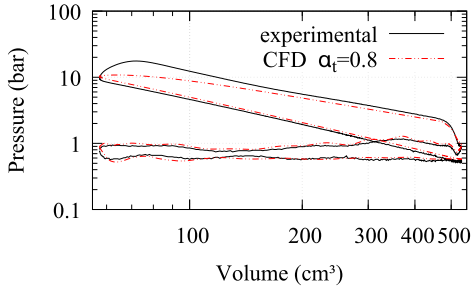

(c) Case 6 (900 rpm; partial load)

Fig. 5. In-cylinder pressures versus displaced volume for cases 1, 2 and 6 simulated with $\alpha_t = 0.8$. Experimental data (solid line), 3D CFD simulation (dashed line). The uncertainty of the piezoelectric pressure sensor is $+/-1\%$.

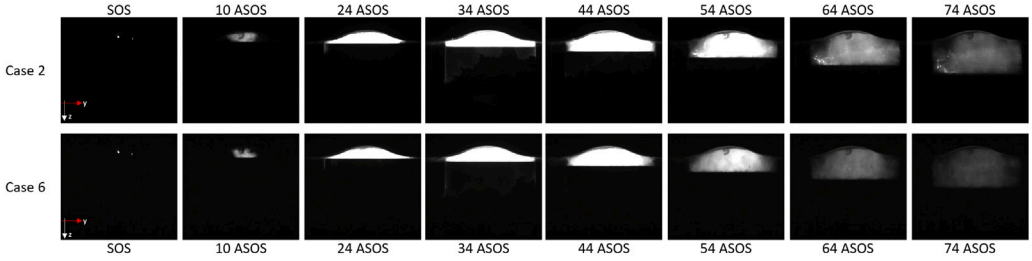

Fig. 6. Natural luminescence combustion images: case 2 (900 rpm; full load) and case 6 (900 rpm; partial load).

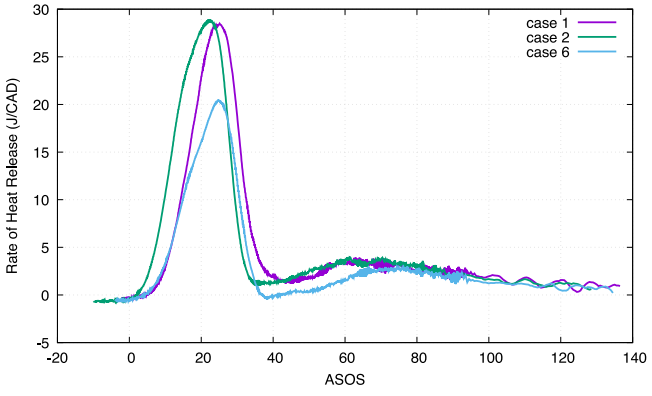

Fig. 7. Rate of Heat Release: case 1 (2000 rpm; partial load), case 2 (900 rpm; full load) and case 6 (900 rpm; partial load).

Table 8
ECFM parameter α_t as function of the ratio turbulent integral length scale and laminar flame thickness.

Case	$\frac{L}{\delta_{fl}}$ [–]	α_t [–]
1 (2000 rpm; full load)	47	0.8
2 (900 rpm; full load)	45	0.9
3 (2500 rpm; full load)	46	0.9
4 (2500 rpm; partial load)	34	1.6
5 (2000 rpm; partial load)	33	1.7
6 (900 rpm; partial load)	24	2.2

4. Conclusions

The main objective of this work was to validate a spray turbulent combustion model for a DISI internal combustion engine fueled with hydrous ethanol. For that, a strategy was proposed to calibrate specific combustion model parameters, in order to describe both full and part load operation. To perform this validation, experimental data obtained on a single-cylinder research engine with optical access were used. The engine operational points were chosen ranging from low to high speed as well as for full and partial loads. This granted the numerical model is not tuned to a particular spray and turbulent combustion pattern.

The hydrous ethanol spray was characterized using a Phase Doppler Interferometer system. Droplets axial velocities, Sauter Mean Diameter and spray cone angle were measured for representative engine operational points in open and quiescent environment. Numerical simulations of the sprays were carried out in order to fit the discrete phase model parameters, which were afterwards used in the simulation of the optical engine.

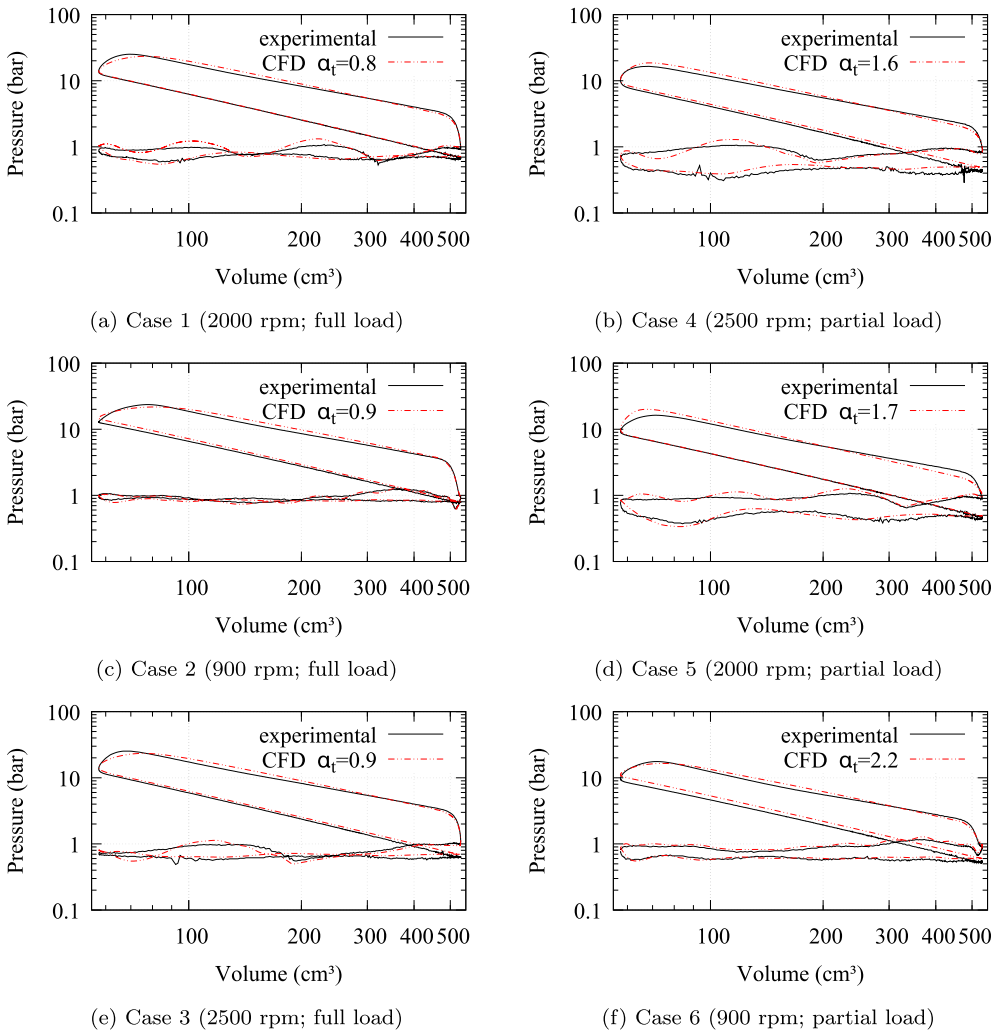

(a) Case 1 (2000 rpm; full load)

(b) Case 4 (2500 rpm; partial load)

(c) Case 2 (900 rpm; full load)

(d) Case 5 (2000 rpm; partial load)

(e) Case 3 (2500 rpm; full load)

(f) Case 6 (900 rpm; partial load)

Fig. 8. In-cylinder pressures using corrected α_t. The uncertainty of the piezoelectric pressure sensor is +/ − 1%.

Table 9
Experimental and 3D CFD simulated IMEP results.

Case	$IMEP_{exp}$ [bar]	$IMEP_{CFD}$ $\alpha_t = 0.8$ [bar]	Absolute deviation [%]	$IMEP_{CFD}$ calibrated α_t [bar]	Absolute deviation [%]
1	4.99 ± 0.16	5.14 ± 0.04	3.01	5.14 ± 0.04	3.01
2	5.02 ± 0.28	5.10 ± 0.04	1.59	5.32 ± 0.05	5.98
3	5.06 ± 0.10	5.33 ± 0.03	5.40	5.38 ± 0.03	6.32
4	3.07 ± 0.08	2.81 ± 0.01	8.63	3.22 ± 0.08	4.89
5	3.02 ± 0.08	2.73 ± 0.05	9.71	3.10 ±0.01	2.65
6	3.03 ± 0.09	2.10 ± 0.27	30.69	2.92 ± 0.01	3.63

Optical techniques for natural luminescence and pressure transducers, were applied to gather experimental data on ethanol turbulent combustion on a DISI engine. These experimental data were compared with the numerical results obtained with the ECFM combustion model.

In order to come up with information missing from the experimental setup, a 1D model was built and calibrated, in an interactive way, using simultaneously results from 3D CFD simulations and acquired experimental data.

The ECFM combustion model was demonstrated a feasible tool to represent an ethanol direct-injection, spray-guided, spark-ignited engine. Herein, a successful approach was proposed to address the model parameters of the ECFM. It was observed that a correction of the turbulence stretch parameter can be done according to the ratio of integral turbulence scale to the laminar flame thickness, at the ignition timing. The CFD simulation of all the six studied cases shown good agreement based on the indicated pressure, for engine speed range from 900 rpm to 2500 rpm as well as load range from 3 bar to 5 bar of IMEP. The deviation between experimental and simulated IMEP is chosen as a measure for the model validity. Doing this, the average value for the absolute deviation, calculated with the six cases, is 9.83% and 4.41% for constant and corrected α_t respectively. If only the low load cases (3 bar IMEP) are taken into account, the average value for the deviations for constant and corrected α_t are 16.34% and 3.72% respectively. These results clearly indicate the improvements delivered by the proposed approach, which is recommended for future investigations.

Declaration of competing interest

The authors declare the following financial interests/personal relationships which may be considered as potential competing interests:

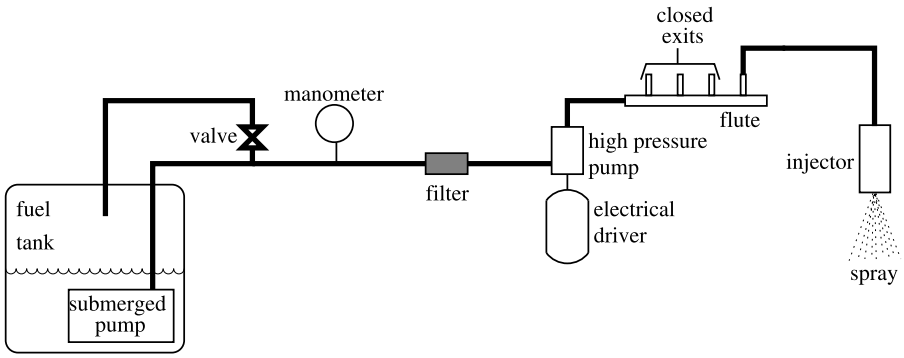

Fig. A.9. Experimental arrangement for spray control.

Guenther Carlos Krieger Filho reports financial support was provided by Peugeot Citroen do Brasil Automoveis Ltda.

Data availability

Data will be made available on request.

Acknowledgments

The authors would like to thank FAPESP, Convergent Science and Peugeot Citroen do Brasil Automoveis Ltda/Stellantis for supporting this research project. This research was funded by São Paulo Research Foundation (FAPESP), Brazil grant number 2013/50238-3. Convergent Science provided CONVERGE licenses and technical support for this work.

Appendix A. Spray modeling

This appendix shows the experimental measurements of the engine's injector and the calibration of CFD models for a better description of the discrete phase.

A.1. Phase doppler interferometer measurements

A Bosch injector type 0261 500 103 – same employed in the optical engine – has been characterized in this study regarding mean drop diameter and droplet distribution. This injector has six exit orifices and was used at 100 bar of pressure injection on the following conditions: the fuel (hydrated ethanol, E95) was injected during 1.5 ms; at the same time (from the start of the injection) 50 ms was counted for the next injection (so the frequency of starting each injection was 20 Hz, simulating a 4T engine at 2400 rpm). The injection pressure after the high pressure pump was maintained at 100 bar during tests. Fig. A.9 shows the experimental arrangement.

To characterize the spray produced by the injector, a Phase Doppler Interferometer (PDI) system from Artium was used. To choose the measurement point in the spray, the procedures described in the [34] were followed, which recommends measurement at an axial distance of 50 mm from the injector tip. Fig. A.10(a) shows a front view of four plumes produced by the injector out of a total of six plumes. This figure illustrates one of the measurement points at the distance recommended by [34]. In Fig. A.10(b) it is possible to observe the distribution of the centers of the six plumes (the footprint of the spray in red dots) in a plane orthogonal to the z axis. The purple dots represent all points where measurements of axial velocity, V_z, and Sauter Mean Diameter, SMD, were taken by PDI System.

The main parameters of the PDI System used were: 500 mm of front focal length, 500 mm of back focal length, slit aperture used of 400 μm, collection angle at 38°, beam waist of 312,6 μm, and frequency shift of 45 MHz (for Doppler signal sampling). Although only axial velocity and diameter were monitored (on channel 1), channel 2 was also used to validate the droplets, once valid ones occurs for the droplets detected on both PDI channels simultaneously.

In order to make the correct acquisition of the spray, the PDI waited 5 ms from the start of the injection to start acquiring and remained acquiring up to 15 ms. The delay of 5 ms is necessary to allow the drops ejected from the injector to reach the measurement point. These times were estimated based on preliminary tests to determine the order of magnitude of the velocities of the drops. Thus, it was possible to calculate the average time it takes to reach the measurement point after its ejection.

The Sauter Mean Diameter (SMD) measured across the spray at 50 mm below the injector tip, were between 22 and 55 μm. These transversal scan point-wise SMD measurements were then converted into a single, line-of-sight SMD value by weighing and normalizing the measurement at each location with its corresponding flux density. The calculated SMD value resulted in 32.2 μm.

Regarding the experimental results obtained with the PDI, shown in Fig. A.11(a), a relative uniformity on SMD is observed for the left plume ($-40 < x < 0$ mm), but there are two higher peaks on the edges of the right plume ($0 < x < 40$ mm). Such results suggest the spray in this plume is dominated by a droplet distribution that is more gnarly than elsewhere in the domain. Such data, before being classified as spurious, must be understood as the result of some irregularity in the injector orifice, something relatively frequent in automotive injectors, as reported in [35]. Regarding the distribution of velocities, Fig. A.11(b), consistency in the results is observed. There are two solid plume, as opposed to conical sprays. There is a greater amount of momentum inside the sprays than in its periphery, where the aerodynamic drag slows down the droplets in the shear layer.

A.2. Ethanol spray characterization

In order to fit the injection model parameters, a numerical PDI was performed. The simulation domain was a cube with a side of 0.3 m, where the top face was assigned as an inlet boundary condition with a pressure of 94 kPa and 296 K of temperature, and the other 5 faces were assigned as outlet with same pressure and temperature. Injector was positioned at the center of inlet face. Other boundary conditions (i.e.injected mass, injection time, injection frequency) were the same as the experiment. The injector input parameters as initial q, SMD and plume orientation were fitted to experimental data as far as possible, using as first value the results obtained on experiment. Ten consecutive cycles were ran to improve the flow field development and predictions of residual gas fraction and residual temperature. Results of the numerical simulations and PDI SMD measurements for the axial velocity (V_z) are shown in Fig. A.11 and the final fitted parameters are shown on Table A.10.

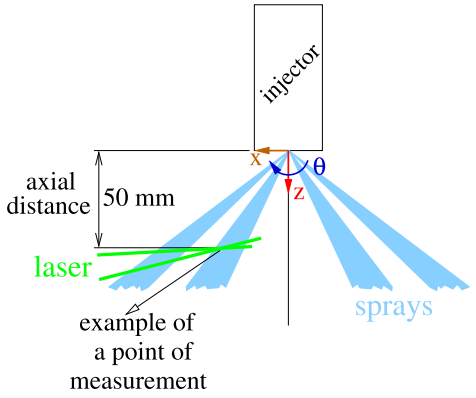

(a) Front view of four plumes produced by the injector.

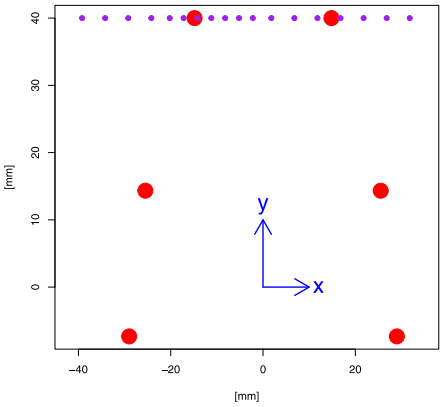

(b) The footprint of the spray plumes in a plane orthogonal to the axial axis at 50 mm from the injector tip.

Fig. A.10. Experimental arrangement for the PDI System measurements.

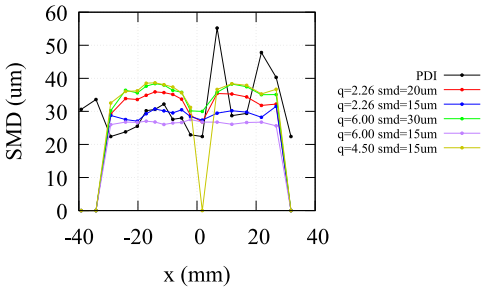

(a) SMD at 50 mm from injector tip as function of the cone angle, initial q and SMD

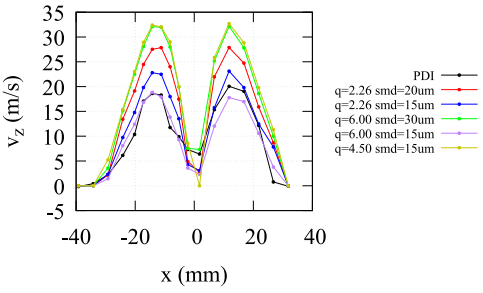

(b) Axial velocity at 50 mm from injector tip as function of the cone angle , initial q and SMD

Fig. A.11. Spray characterization numerical and experimental (PDI)

Table A.10
Fitted values for spray modeling.

Sauter mean diameter [μm]	15
Cone angle [°]	20
Rosin-Rammler's q	2.26

Appendix B. 1D engine model

B.1. 1D CFD gas exchange model

In order to calculate the mass flow rate (crank angle resolved) at the cylinder head boundaries – which are imposed as boundary condition in the 3D CFD model – an one-dimensional (1D) gas exchange model of the engine was built. Intake and exhaust head ports were modeled with the aid of a 3D CAD model of the head ducts, from which measurements (length and cross-sectional area) were taken. Measurements of the pipe length between the intake pressure sensor and head inlet, as well as the pipe between head outlet and exhaust pressure sensor, were taken directly from the engine. Valve lift profiles were provided by the engine manufacturer (AVL List GmbH), as well as engine's main dimensions (bore, stroke, connecting rod length etc.).

A numerical flow bench simulation of the cylinder head was conducted in both 1D and 3D models. Air mass flow results for lifts between 1 mm and 10 mm, in steps of 1 mm, were compared between both 1D and 3D. The discharge coefficients in the 1D model were multiplied by the ratio between 3D and 1D air mass flow rates. The flow bench simulation was re-run in 1D to confirm the new discharge coefficient values. Since this engine presents some backflow in some operating points, both forward and reverse discharge coefficients were calculated using this methodology. Fig. B.12 shows the discharge coefficient to intake and exhaust valves in both forward and reverse directions.

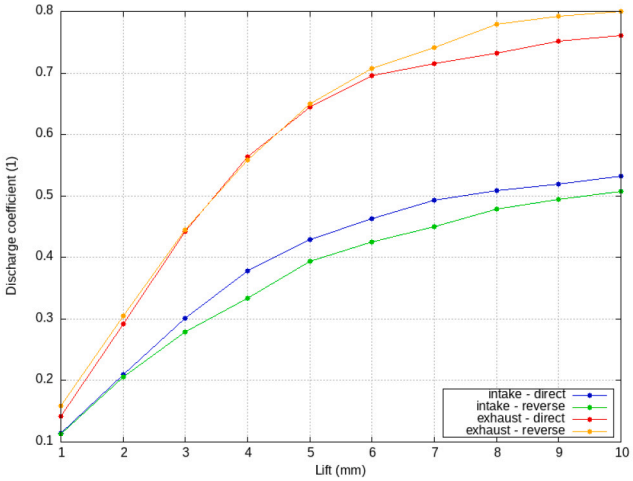

Fig. B.12. Discharge valve coefficients against the valve lift distance. Numerical flow bench results for intake and exhaust valves in both forward and reverse directions.

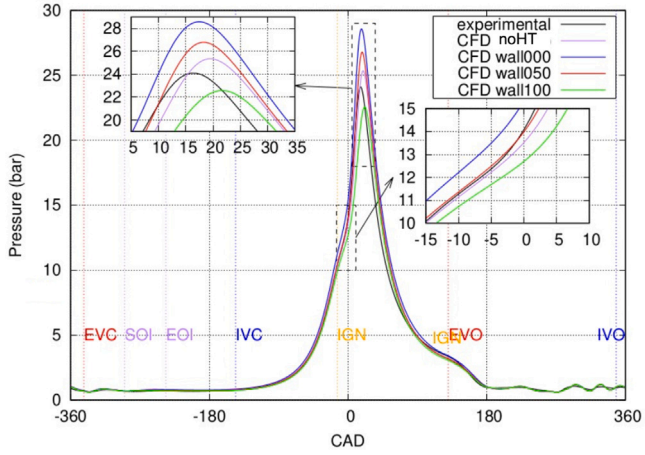

Fig. B.13. Effect of energy source for fuel evaporation in the in-cylinder pressure.

B.2. 1D thermal model

Imposed wall temperatures or correlation [36] were used to model heat transfer between the fluid and pipe/ports walls. Friction losses at the ports were set to zero, since they are already accounted for in the valves discharge coefficients.

Optical engines, as the one employed in this work, are known for having a large crevice volume, since the piston ring should not contact the sapphire cylinder walls. The crevice volume was also accounted for by summing its value to the dead volume and calculating an equivalent/effective compression ratio.

The intake and exhaust pressure traces were used as boundary conditions, in order to avoid the uncertainties of simulating the whole intake and exhaust ducts, which are relatively long in this engine. In-cylinder pressure trace from motored operation was used for calibration and validation of in-cylinder heat transfer coefficients and wall temperatures. Here, the Woschni [36] in-cylinder heat transfer model was used. For fired operation, in-cylinder pressure trace was used to calculate the heat release rate. This methodology is usually called TPA [37].

Due to thermal and lubrication limitations of a transparent engine, specially in fired operation, this engine cannot run for long. Thus, it usually never reaches steady state. Since fuel and air flow rates are constantly changing during operation, the values measured around the time of the reference cycle were used for model correlation and also to impose the correct amount of injected fuel. Another parameter that was analyzed is the source of energy for fuel vaporization. A few tests were conducted (Fig. B.13) allowing the fuel to evaporate without using energy from walls or gas phase (CFD noHT), using energy only from the gas phase (CFD wall000), using half of gas and half of wall (CFD wall050) and using energy only from wall (CFD wall100). The best result regarding the pumping phase of the engine was using an evenly distributed between gas phase and wall heat transfer (CFD wall050).

At the end of each 1D simulation case, the intake both mass flow rate and temperature as well as the exhaust pressure traces were generated and applied onto the 3D CFD simulation as boundary conditions. Fig. B.14 shows the boundary conditions used in Case 1.

Appendix C. Grid independence and convergence verification

A mesh independence study was conducted using the Grid Convergence Index (GCI) [38] using IMEP values for the baseline case 6 (900 rpm/3 bar). Table C.11 shows grid values and its IMEP value. Rules for grid refinement were kept the same for all cases.

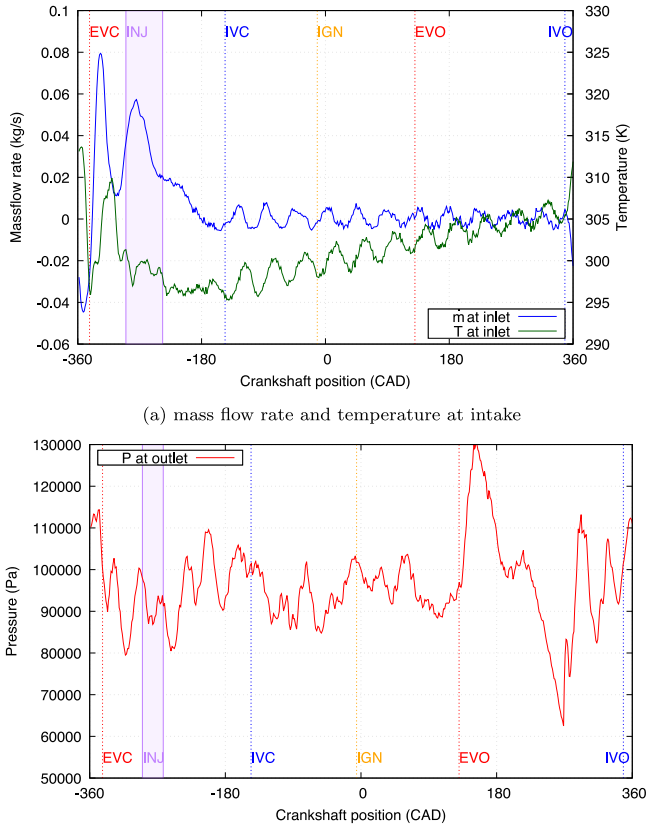

(a) mass flow rate and temperature at intake

(b) pressure at exhaust

Fig. B.14. Case 1; Inlet and exhaust boundary conditions for the 3D CFD simulation.

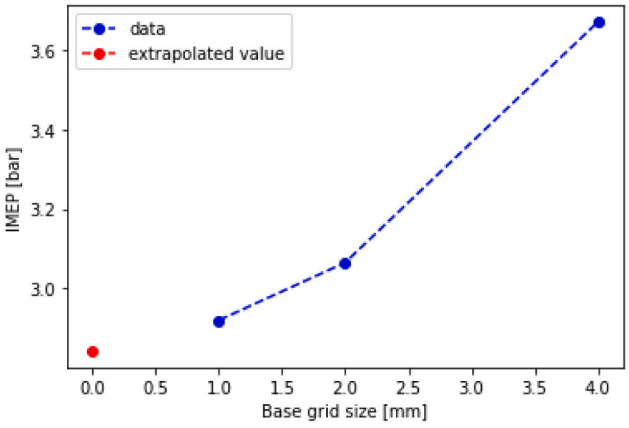

Fig. C.15. IMEP value as function of cylinder grid size and extrapolated value using Richardson extrapolation.

Table C.11
Grids description and IMEP values used for GCI calculations.

Grid	Cylinder grid size [mm]	IMEP [bar]
Coarse	4	3.670
Mid	2	3.065
Fine	1	2.920

The GCI can be computed by

$$GCI_{12} = \frac{F_s \left| \frac{f_1 - f_2}{f_1} \right|}{2^p - 1} \tag{C.1}$$

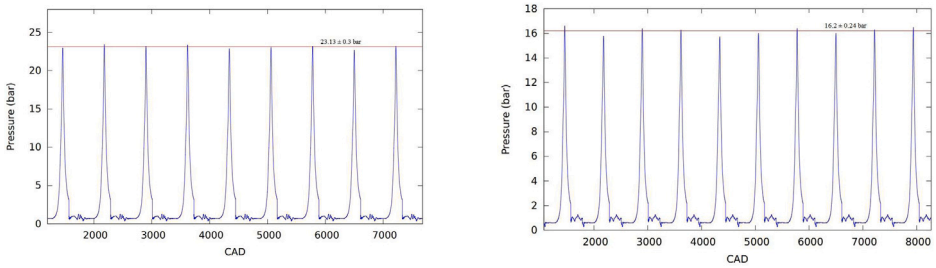

(a) Case 1. (b) Case 6.

Fig. C.16. Cycle to cycle pattern of simulated in-cylinder pressure. Horizontal line is the averaged peak pressure calculated over the last ten cycles.

$$GCI_{23} = \frac{F_s \left| \frac{f_2 - f_3}{f_2} \right|}{2^p - 1} \tag{C.2}$$

where F_s is the factor of safety, f_1, f_2 and f_3 are the IMEP for fine, middle and coarse grids, respectively. p is the order of convergence, that can be calculated by

$$p = \frac{ln\left(\frac{f_3 - f_2}{f_2 - f_1}\right)}{ln(2)} \tag{C.3}$$

Using a F_s of 1.25 (recommended for 3 grids), the order of convergence p are 1.72 and the calculated GCI_{12} and GCI_{23} are 0.033 and 0.102. The ratio $\frac{GCI_{23}}{GCI_{12}2^p}$ is equals to 0.943, suggesting that the solutions were close to the asymptotic range of convergence.

The value exact value can be estimated using Richardson extrapolation (Eq. (C.4)).

$$f_0 = f_1 + \frac{f_1 - f_2}{2^p - 1} \tag{C.4}$$

For case 1, the exact value is 2.843 bar with an error band of 9.32% (see Fig. C.15). One way to show the presented results are converged is to observe the numerical cycle to cycle variation of one representative quantity. In this way, it is reported a sequence of the last ten simulated full cycles (720 CAD) for cases 1 and 6, see Fig. C.16. The averaged value of the peak pressure is represented by the red horizontal line. It is easy to see the numerical results oscillate above and below the averaged value. This indicates the numerical error is not accumulated but rather oscillates around the averaged value. The average and standard deviation of IMEP are evaluated over the last ten simulated cycles and shown on Table 9. The standard deviation of the numerical simulation is about one order of magnitude lower as the experimental ones. This ensures the numerical results are reliable enough.

Error accumulation analysis is carried out following method presented in [39]. The method was applied in the 10th. simulated engine cycle (see Fig. C.16). The relative error of integration is evaluated based on the averaged number of cell (N_{cells}) as

$$S_{err} = 3 \times \left(\frac{1}{\sqrt[3]{Ncells}} \right)^2 \tag{C.5}$$

The allowable value of the total error S_{max} was chosen 10% [39, 40], and the obtained results from the error accumulation data are summarized on Table C.12

The reliability parameter (R_s) for this study is close to the value chosen in [39], i.e. $R_s = 0.45$. According to the obtained results, the stochastic error accumulation indicates that the applied approach is suitable to address the selected object of study.

Table C.12
Error accumulation.

	Case 1	Case 6
Averaged number of cells (N_{cells})	258554	245820
Averaged number of Navier–Stokes iterations per engine cycle	42360	61362
Relative error (S_{err})	7.39e−4	7.64e−4
Maximum allowed iterations (n_{max})	18302	17110
Reliability (R_s)	0.43	0.28

References

[1] C. Panoutsou, S. Germer, S. Karka, Y. Kroyan, K. Wojcieszyk, P. Marchand, I. Landalv, Advanced biofuels to decarbonise European transport by 2030: Markets, challenges, and policies that impact their successful market uptake, Energy Strategy Rev. 34 (2021) 100633, http://dx.doi.org/10.1016/j.esr.2021.100633.

[2] Yongming Bao, Qing Nian Chan, Sanghoon Kook, Evatt Hawkes, Spray penetrations of ethanol, gasoline and iso-octane in an optically accessible spark-ignition direct-injection engine, SAE Int. J. Fuels Lubricants 7 (3) (2014) 1010–1026, http://www.jstor.org/stable/26273739.

[3] J. Serras-Pereira, P.G. Aleiferis, D. Richardson, An analysis of the combustion behavior of ethanol, butanol, iso-octane, gasoline and methane in a direct-injection spark-ignition research engine, Combust. Sci. Technol. 185 (2013) 484–513.

[4] F.L. Sacomano Filho, et al., A new robust modeling strategy for multi-component droplet heat and mass transfer in general ambient conditions, Int. J. Heat Mass Transfer 194 (2022) http://dx.doi.org/10.1016/j.ijheatmasstransfer.2022.123102.

[5] F.P. Martins, C.R. de Andrade, V.L. Penteado, Simulation and analysis of direct injection strategies for hydrous ethanol in internal combustion engines, Int. J. Eng. Innov. Technol. 3 (2014) 207–215, ISSN: 2277-3754.

[6] Y. Huang, G. Hong, R. Huang, Investigation to charge cooling effect and combustion characteristics of ethanol direct injection in a gasoline port injection engine, Appl. Energy (2015) http://dx.doi.org/10.1016/j.apenergy.2015.09.059.

[7] J.G.C. Baeta, M. Pontoppidan, T.R.V. Silva, Exploring the limits of a downsized ethanol direct injection spark ignited engine in different configurations in order to replace high-displacement gasoline engines, Energy Convers. Manag. 105 (2015) 858–871, http://dx.doi.org/10.1016/j.enconman.2015.08.041.

[8] P.G. Aleiferis, J. Serras-Pereira, D. Richardson, Characterisation of flame development with ethanol, butanol, iso-octane, gasoline and methane in a direct-injection spark ignition engine, Fuel (2013) http://dx.doi.org/10.1016/j.fuel.2012.12.088.

[9] M.M. Koupaie, A. Cairns, H. Vafameher, T.D.M. Lanzanova, A study of hydrous ethanol combustion in an optical central direct injection spark ignition engine, Appl. Energy 237 (2019) 258–269, http://dx.doi.org/10.1016/j.apenergy.2018.12.093.

[10] Y. Huang, et al., Spray and evaporation characteristics of ethanol and gasoline direct injection in non-evaporating, transition and flash-boiling conditions, Energy Convers. Manage. (2016) http://dx.doi.org/10.1016/j.enconman.2015.10.081.

[11] M. Battistoni, F. Mariani, F. Risi, C. Poggiani, Energy Procedia 82 (2015) 424–431.

[12] M. Rahimi Boldaji, A. Sofianopoulos, S. Mamalis, B Lawler, A CFD investigation of the effects of fuel split fraction on advanced low temperature combustion: Comparing a primary reference fuel blend and ethanol, Front. Mech. Eng. 4 (2018) 6, http://dx.doi.org/10.3389/fmech.2018.00006.

[13] N. Giramondi, D. Konstanzer, A. Erlandsson, Evaluation of the Ethanol-Diesel Spray Interaction during Ignition in a Dual-Fuel DICI Engine Using an Experimentally Validated CFD Model, SAE Technical Paper 2021-01-0521, 2021, http://dx.doi.org/10.4271/2021-01-0521.

[14] Y. Zhuang, G. Zhu, Z. Gong, C. Wang, Y. Huang, Experimental and numerical investigation of performance of an ethanol-gasoline dual-injection engine, Energy 186 (2019) 115835, http://dx.doi.org/10.1016/j.energy.2019.07.165.
[15] Y. Yu Liang, et al., Analysis on the combustion process of the ethanol - diesel direct injection engine with simultaneous diesel and ethanol injection (with ethanol injection starting point earlier than the diesel injection starting point), in: Advances in Engineering Research, Vol. 150, Atlantis Press, 2018.
[16] G.K.K. Prashant, D.B. Lata, P.C. Joshi, Investigations on the effect of ethanol blend on the combustion parameters of dual fuel diesel engine, Appl. Therm. Eng. 96 (2016) 623–631, http://dx.doi.org/10.1016/j.applthermaleng.2015.11.051.
[17] A.A. Yusuf, F.L. Inambao, Effect of low bioethanol fraction on emissions, performance, and combustion behavior in a modernized electronic fuel injection engine, Biomass Convers. Biorefinery 11 (2021) 885–893, http://dx.doi.org/10.1007/s13399-019-00519-w.
[18] Xiuyong Shi, et al., Three-dimensional simulation analysis of the effect of hydrous ethanol and exhaust gas recirculation on gasoline direct injection engine combustion and emissions, J. Energy Res. Technol. 144 (2022) http://dx.doi.org/10.1115/1.4052861.
[19] S. Padala, et al., Effect of ethanol port-fuel-injector position on dual-fuel combustion in an automotive-size diesel engine, Energy Fuels 28 (2014) 340–348, http://dx.doi.org/10.1021/ef401479s.
[20] F.F. Zulkurnai, et al., Simulation of combustion process of diesel and ethanol fuel in reactivity controlled compression ignition engine, CFD Lett. 13 (2) (2021) 1–11, http://www.akademiabaru.com/cfdl.html.
[21] O. Colin, A. Benkenida, The 3-zones extended coherent flame model (ECFM3z) for computing premixed/diffusion combustion, Oil Gas Sci. Technol. 59 (6) (2004) 593–609.
[22] O. Colin, A. Benkenida, C. Angelberger, 3D modeling of mixing, ignition and combustion phenomena in highly stratified gasoline engines, Oil Gas Sci. Technol. 58 (2003) 47–62.
[23] E.R. Malheiro de Oliveira, C.H. Rufino, P.T. Lacava, Effects of direct injection and mixture enleament on the combustion of hydrous ethanol and an ethanol-gasoline blend in an optical engine, FUEL 327 (2022) 125137.
[24] C.A.R. Duarte, P.T. LACAVA, Combustion characterization of commercial ethanol fuels in an optical research SI ignition engine for different injection strategies, J. Bra. Soc. Mech. Sci. Eng. 44 (2022) 232.
[25] K.J. Richards, P.K. Senecal, E. Pomraning, CONVERGE 3.1.6, in: Convergent Science, Madison, WI, 2021.
[26] V. Knop, A. Benkenida, S. Jay, Colin. O., Modelling of combustion and nitrogen oxide formation in hydrogen-fuelled internal combustion engines within a 3D CFD code, Int. J. Hydrogen Energy 33 (2008) 5083–5097.
[27] C. Meneveau, T. Poinsot, Stretching and quenching of flamelets in premixed turbulent combustion, Combust. Flame 86 (4) (1991) 311–332, http://dx.doi.org/10.1016/0010-2180(91)90126-V.
[28] O. Colin, K. Truffin, A spark ignition model for large eddy simulation based on an FSD transport equation (ISSIM-LES), Proc. Combust. Instit. 33 (2) (2011) 3097–3104, http://dx.doi.org/10.1016/j.proci.2010.07.023.
[29] C. Angelberger, T. Poinsot, B. Delhaye, Improving near-wall combustion and wall heat transfer modeling in SI engines computations, SAE Pap. (1997) 972881, http://dx.doi.org/10.4271/972881.
[30] M. Metghalchi, J.C. Keck, Burning velocities of mixtures of air and methanol, isooctane and indolene at high pressures and temperatures, Combust. Flame 48 (1982) 191–210, http://dx.doi.org/10.1016/0010-2180(82)90127-4.
[31] Z. Han, R.D. Reitz, Turbulence modeling of internal combustion engines using RNG k-ε models, Combust. Sci. Technol. 106 (4–6) (1995) 267–295, http://dx.doi.org/10.1080/00102209508907782, 1995.
[32] R.C. Liu, L.E. Jia-Ling, S.H. Yang, Z.H. Zheng, Y. Huang, Application of KH-rt model in process of spray jet breakup in across-flow, J. Propul. Technol. 38 (7) (2017) 1595–1602.
[33] A.A. Amsden, P.J. O'Rourke, T.D. Butler, KIVA-II: A Computer Program for Chemically Reactive Flows with Sprays, Technical Report LA-11560-MS, Los Alamos National Laboratory, 1989.
[34] D.L.S. Hung, D.L. Harrington, A.H. Gandhi, L.E. Markle, S.E. Parrish, J.S. Shakal, H. Sayar, S.D. Cummings, J.L. Kramer, Gasoline Fuel Injector Spray Measurement and Characterization - a New SAE J2715 Recommended Practice, in: SAE Technical Paper Series 2008-01-1068, 2008.
[35] S.E. Parrish, The influence of nozzle hole manufacturing methods on spray characteristics of multi-hole gasoline fuel injectors, in: 14 Th Triennial International Conference on Liquid Atomization and Spray Systems, ICLASS, Chicago, IL, USA, July (2018), 2018, pp. 22–26.
[36] G. Woschini, J. Fieger, Experimental investigation of the heat transfer at normal and knocking combustion in spark ignition engines, MTZ 43 (1982) 63–67.
[37] Gamma Technologies, GT-suite engine performance application manual, 2020.
[38] Roache, J. Patrick, Perspective: A method for uniform reporting of grid refinement studies, J. Fluids Eng. 116 (1994) 405–413.
[39] N.N. Smirnov, et al., Hydrogen fuel rocket engines simulation using LOGOS code, Int. J. Hydrogen Energy 39 (20) (2014) 10748–10756.
[40] N.N. Smirnov, et al., Accumulation of errors in numerical simulations of chemically reacting gas dynamics, Acta Astronaut. 117 (2015) 338–355.